

Vapor-Phase Infiltration of Polymer of Intrinsic Microporosity 1 (PIM-1) with Trimethylaluminum (TMA) and Water: A Combined Computational and Experimental Study

Yifan Liu, Emily K. McGuinness, Benjamin C. Jean, Yi Li, Yi Ren, Beatriz G. del Rio, Ryan P. Lively, Mark D. Losego,* and Rampi Ramprasad*



Cite This: <https://doi.org/10.1021/acs.jpcb.2c01928>



Read Online

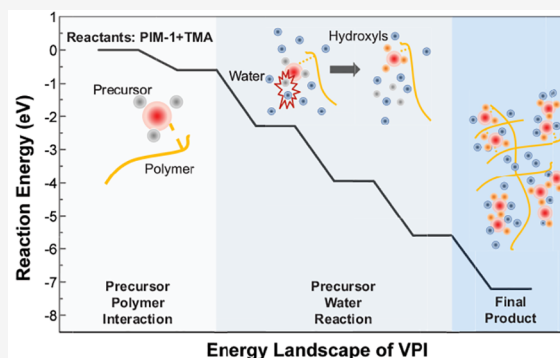
ACCESS |

Metrics & More

Article Recommendations

Supporting Information

ABSTRACT: Vapor-phase infiltration, a postpolymerization modification process, has demonstrated the ability to create organic–inorganic hybrid membranes with excellent stability in organic solvents while maintaining critical membrane properties of high permeability and selectivity. However, the chemical reaction pathways that occur during VPI and their implications on the hybrid membrane stability are poorly understood. This paper combines *in situ* quartz crystal microbalance gravimetry (QCM) and *ex situ* chemical characterization with first-principles simulations at the atomic scale to study each processing step in the infiltration of polymer of intrinsic microporosity 1 (PIM-1) with trimethylaluminum (TMA) and its co-reaction with water vapor. Building upon results from *in situ* QCM experiments and SEM/EDX, which find TMA remains within PIM-1 even under long desorption times, density functional theory (DFT) simulations identify that an energetically stable coordination forms between the metal–organic precursor and PIM-1’s nitrile functional group during the precursor exposure step of VPI. In the subsequent water vapor exposure step, the system undergoes a series of exothermic reactions to form the final hybrid membrane. DFT simulations indicate that these reaction pathways result in aluminum oxyhydroxide species consistent with *ex situ* XPS and FTIR characterization. Both NMR and DFT simulations suggest that the final aluminum structure is primarily 6-fold coordinated and that the aluminum is at least dimerized, if not further “polymerized”. According to the simulations, coordination of the aluminum with at least one nitrile group from the PIM-1 appears to weaken significantly as the final inorganic structure emerges but remains present to enable the formation of the 6-fold coordination species. Water molecules are proposed to complete the coordination complex without further increasing the aluminum’s oxidation state. This study provides new insights into the infiltration process and the chemical structure of the final hybrid membrane including support for the possible mechanism of solvent stability.



INTRODUCTION

Chemical separations account for over 10% of the world’s energy consumption.¹ Today, most separations are accomplished with energy-intensive thermal means. Chemical separation via membrane technologies can reduce energy costs by up to 90%. For instance, the separation of benzene derivatives requires approximately 430 TWh of energy each year;¹ membrane processes such as organic solvent nanofiltration (OSN) and organic solvent reverse osmosis (OSRO) can potentially drive this energy cost down by an order of magnitude.² Though commercial solutions are available for separating aqueous streams, challenges still exist for separating organic solutions. New membrane materials like zeolites,³ porous organic cages,⁴ metal–organic frameworks,⁵ and cross-linked polymer networks⁶ are being developed for organic solvent separation technologies.^{2,7} Inorganic membranes, such as zeolites, can be stable in organic solvents but are costly and difficult to scale-up in a defect-free manner.⁶ Solution-

processable polymers can be processed into a variety of membrane structures (thin film composites, hollow fibers, etc.) which are highly permeable and selective, but these materials do not display the same level of stability in organic solutions as inorganic materials, limiting the scope of their use. One well-established approach to increase the chemical stability of polymeric membranes is cross-linking.⁶ However, cross-linking typically requires chemical processing that makes it challenging to maintain the polymer’s macroscopic form, limiting the form factors accessible through this technique (e.g., hollow fiber spinning). As a result, several alternative postfabrication techniques have been developed to enhance the solvent stability of polymer membranes.^{2,8,9} However, these proce-

Received: March 20, 2022

Revised: July 18, 2022

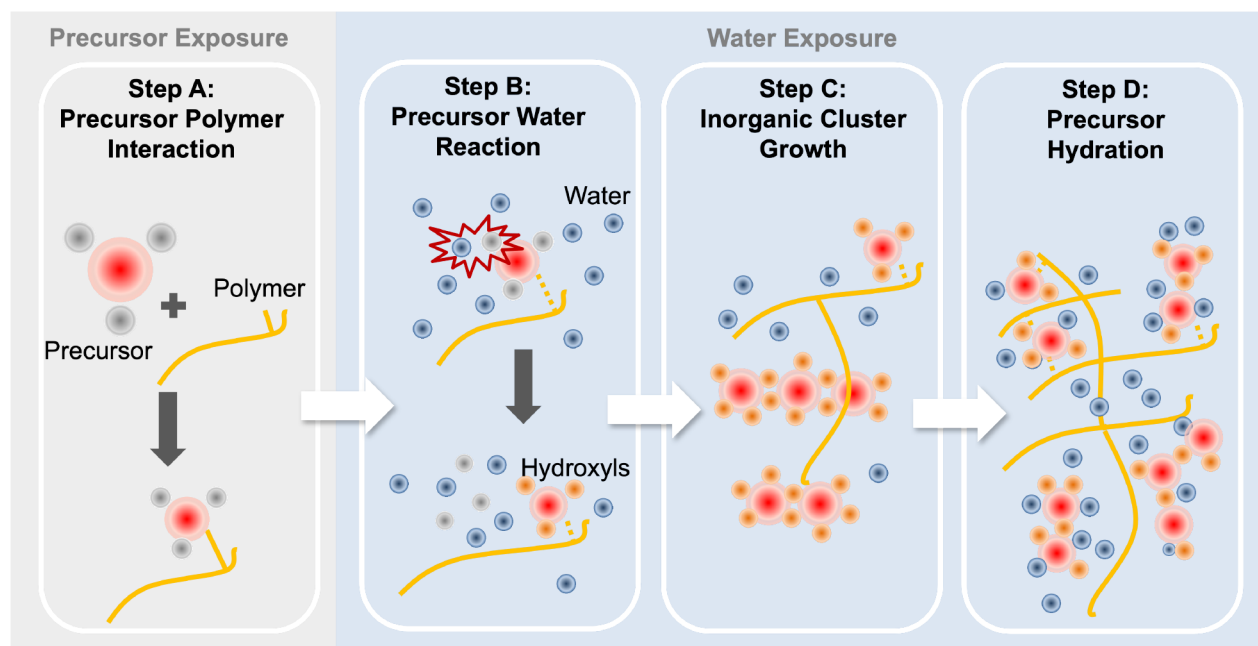


Figure 1. Schematic of the proposed processes that occur during vapor-phase infiltration (VPI). (Step A) The metal–organic precursor interacts with the polymer during the precursor exposure. (Step B) Upon water vapor exposure, the precursor becomes oxidized to form metal hydroxide clusters (the gray dots [ligands] of the precursor react with the blue water molecules to become orange dots [hydroxyls]). (Step C) These hydroxide clusters coordinate with each other to grow into larger oxyhydroxide inorganic clusters. (Step D) Further coordination occurs via hydration binding of additional water molecules.

dures often lead to defect formation and significant changes in the microscopic structure of the membrane.

Polymers of intrinsic microporosity (PIMs) are of interest for organic solvent separation because of their inherent interconnected microporosity.¹⁰ PIM-1, a prototypical PIM, is a rigid, solution-processable, glassy polymer with a high degree of microporosity (pores less than 2 nm in ambient conditions).¹¹ The microporosity and narrow pore size distribution of PIM-1 result in its size-based molecular-sieving capabilities. In addition, because of its high free volume, PIM-1 displays a high diffusion coefficient, yielding high flux and eventually high retention nanofiltration membranes.¹² However, PIM-1 has reduced selectivity when subjected to plasticizing solvents and dissolves in the presence of good solvents.^{8,10,13} The instability of PIM-1 in certain solvents prevents it from being broadly applied to organic solvent separation processes.

Vapor-phase infiltration (VPI) is a gas-phase method for infusing metal–organic constituents into a polymer and forming an organic–inorganic hybrid material.^{14–18} Recently, VPI has shown promise for creating a variety of hybrid membrane materials such as metal oxide/PIM-1,^{19,20} poly(ether sulfone)/graphite,²¹ and carbon molecular sieves.²² Figure 1 shows a schematic of the processes that are proposed to occur during VPI. First, the polymer is placed inside an evacuated reactor and exposed to a static environment containing a vapor-phase metal–organic precursor for a period of time (step A in Figure 1), allowing it to sorb into the polymer. Depending upon a number of parameters (polymer chemistry, polymer morphology, precursor chemistry, temperature, pressure, etc.), this metal–organic precursor will dissolve, diffuse, and/or react to varying extents. Typically, this exposure is followed by a precursor removal step in which the excess precursor in the environment is removed. In this

step, any precursor that is not chemically interacting with the polymer starts to desorb. The amount of precursor that desorbs by the end of this step depends upon the out-diffusion kinetics and process time. To trap these inorganic precursor molecules (if desired) and create an air-stable material, a co-reactant (commonly water vapor) is introduced to form a nonvolatile inorganic cluster (commonly a metal oxide or oxyhydroxide) that is homogeneously included at the molecular level within the polymer (steps B–D in Figure 1). A single VPI exposure cycle can be adequate to achieve inorganic loadings of several weight percentages within the subsurface or bulk of a polymer.^{23,24}

Recently, VPI has been used to create the hybrid membranes of AlO_x -PIM-1 from infiltration of trimethylaluminum (TMA) and water vapor into PIM-1.²⁰ AlO_x -PIM-1 exhibits enhanced chemical stability, uninterrupted microporosity, and improved organic solvent nanofiltration performance, even in good solvents for the polymer. In their work, McGuinness et al.²⁰ proposed a reaction mechanism whereby TMA first forms an adduct with the PIM-1 nitrile group. This adduct subsequently reverses upon the introduction of water, forming an unbound aluminum oxide/hydroxide species. However, because of a lack of available *in situ* experimental capabilities, the authors were unable to directly probe these chemical interactions and reaction processes. Additionally, the authors were unable to identify precisely the mechanism of this enhanced solvent stability.

Indeed, the interactions between polymer and metal–organic precursors in a VPI process are complicated. For example, the underlying reaction mechanisms for VPI of TMA into poly(methyl methacrylate) (PMMA) have taken several years and multiple publications to elucidate.^{25–28} Determining the chemical structure of the resultant inorganic within the polymer is equally challenging. Recent experimental work

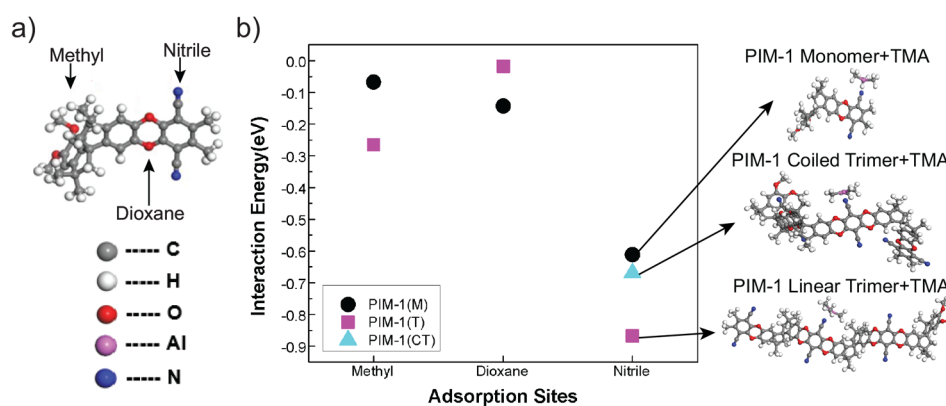


Figure 2. (a) Illustration of different adsorption sites on the monomer of PIM-1 (nitrile, methyl, and dioxane). (b) Interaction energy of TMA on different adsorption sites on PIM-1 for the three models considered: monomer molecule (black dots), trimer molecule (magenta squares), and coiled trimer molecule (cyan triangles).

using EXAFS and high energy X-ray scattering with pair distribution function analysis (HEX-PDF) has begun to reveal the complex atomic scale structure that these infiltrated inorganic clusters can have, but much is still unknown.^{29,30} Understanding the reaction pathways, especially the reaction kinetics, is key for industrial scale up while understanding the inorganic's structure will inform structure–property relationships in these hybrid materials, revealing new applications and providing explanations for already reported materials properties and phenomena.

Computational methods can complement experimental investigations to help clarify these complex reactions and the resultant organic–inorganic hybrid structures created during VPI. Accurate *ab initio* simulations using density functional theory (DFT) have already been used to complement VPI experimental works by simulating FTIR spectra for comparison with *in situ* FTIR studies,²⁵ understanding adsorption energies, free energies, energy barriers, and total energy gain for the potential reaction pathways between VPI precursors and different functional groups,³¹ and predicting the temperatures at which the forward and reverse reactions between VPI precursors and polymers reach a balance point.³²

In the present work, we explore and refine the reaction pathways and final hybrid material structure proposed by McGuinness et al.²⁰ for VPI of TMA + H₂O into PIM-1. The goal of this paper is to combine *in situ* quartz crystal microbalance (QCM) experiments, *ex situ* chemical characterization (NMR, XPS, FTIR), and DFT simulations in an efficient way to understand the interactions among PIM-1, TMA, and derived products throughout the VPI process, the chemical structure of the final products, and how these structures may evoke solvent stability. First, insight into TMA-(PIM-1) chemical interactions during the precursor exposure step of the VPI process (step A in Figure 1) is provided through DFT, with the presence of interactions confirmed via *in situ* QCM, and *ex situ* SEM/EDX experiments utilizing long precursor desorption times. Changes in chemical structure during the water exposure step are then explored via DFT by studying the co-reaction of the TMA-(PIM-1) structure with water molecules (step B in Figure 1). The reaction energy path and electron density difference are computed to analyze the interaction between PIM-1 and metal precursor throughout the whole process. To elucidate the ultimate structure of the final products after PIM-1 infiltration with TMA and water, *ex situ* solid-state NMR spectroscopy, FTIR, and X-ray photo-

electron spectroscopy (XPS) are employed to guide additional simulation. This combined experimental and computational approach uncovers final aluminum oxyhydroxide species that likely form via inorganic cluster growth and precursor hydration (steps C and D in Figure 1). Our findings provide an understanding of the chemical structures arising in the TMA/PIM-1 VPI system and a pathway for guiding future characterization of the formation of hybrid organic–inorganic membranes via VPI using DFT to access processing steps challenging to evaluate with experimental techniques and vice versa.

METHODOLOGY

Computational Methods. In this work, we employed the Vienna Ab Initio Simulation Package (VASP)^{33–36} for DFT calculations, and the ion–electron interaction was modeled using the projector-augmented wave (PAW) methodology.³⁷ The Perdew–Burke–Ernzerhof (PBE)³⁸ exchange–correlation (XC) function was used to treat the quantum mechanical part of the electron–electron interactions. The van der Waals DF2 dispersion corrections,^{39,40} known to be important for stabilizing soft materials dominated by nonbonding interactions like polymers,⁴¹ were included.

Before studying the VPI process, we needed to develop a representative model of PIM-1 suitable for DFT simulation, as none currently exists in the open literature. Because of the complexity and porosity of PIM-1, careful analysis of the polymer and selection of the representative atomic model was needed. Because DFT is computationally expensive, with a computational cost increasing cubically with system size, polymer chains of lengths comparable to experimental conditions are not feasible to study.⁴² To efficiently balance realistic conditions and computational cost, a study of the effect of molecular size and morphology on total energy was conducted and is reported in the Supporting Information. From these results, three different atomistic models for PIM-1 were selected for VPI process analysis:⁴² (1) the monomer molecule (PIM-1(M) in Figure 2), (2) the linear trimer molecule (PIM-1(T) in Figure 2), and (3) the coiled trimer molecule (PIM-1(CT) in Figure 2). Although the first two models were obtained by direct relaxation using DFT, the latter structure involved an initial classical molecular dynamics simulation at 600 and 300 K for 50 ps each to allow the system

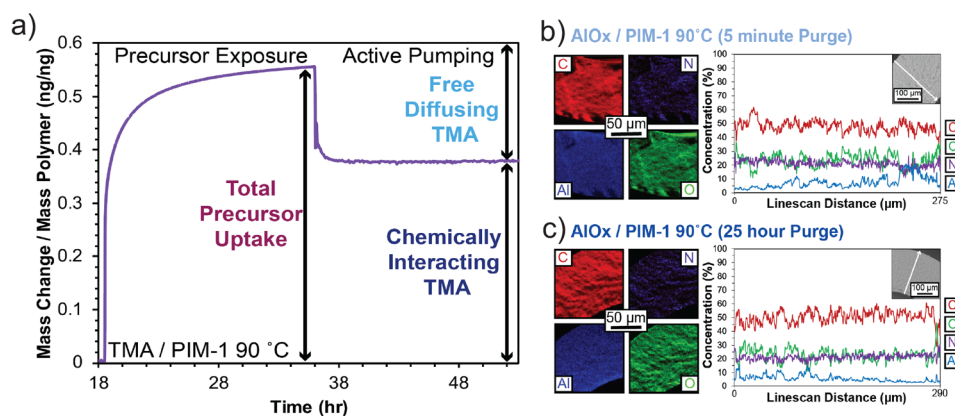


Figure 3. (a) *In situ* quartz crystal microbalance gravimetry (QCM) data showing the mass uptake (normalized to polymer mass) during the TMA sorption (exposure) and desorption (active pumping) portions of infiltration of PIM-1 with TMA at 90 °C.⁴⁶ SEM/EDX cross-sectional maps and line scans of inorganic loading for PIM-1 membranes that were actively purged for (b) 5 min and (c) 25 h.

to coil.⁴² More details about the model preparation are described in the [Supporting Information](#).

Experimental Methods. Vapor-phase infiltration of hollow fiber membranes and thin films on silicon wafers was conducted in a custom-built hot-walled reactor approximately 0.03 m³ in volume. The infiltration process was automated using a custom Labview control software.⁴³ To reset the polymer structure prior to infiltration, PIM-1 was soaked in methanol for at least 2 h and then dried in a fume hood for 30 min.⁴⁴ PIM-1 was then placed within the reactor (heated to 90 °C) which was purged with 250 sccm of ultrahigh purity (UHP) nitrogen from a nitrogen generator (On Site Gas Systems, <10 ppm of O₂) for 5 h to remove excess methanol and water. The chamber was then evacuated via a rotary vane pump to rough vacuum (~30 mTorr) and isolated. Into the static environment was introduced approximately 0.3 Torr of TMA (TMA, Strem Chemicals, 98%, DANGER: pyrophoric). This environment was held static for 5 h with a chamber leak rate of approximately 2 mTorr/min. The chamber was then purged with nitrogen once again for either 5 min (“short purge” experiments) or 25 h (long purge experiments) before being evacuated to rough vacuum. The chamber was isolated once more and room temperature deionized water vapor of approximately 1.8 Torr was introduced. This environment was kept static for 5 h before a final purge step occurred. The chamber pressure was recorded using a Baratron capacitance manometer and the pressure curves for each run are provided in [Figure S6a](#). More details about the experimental methods including polymer synthesis, thin film preparation, and characterization (TGA, FTIR, QCM, NMR, XPS, etc.) can be found in the [Supporting Information](#).

RESULTS AND DISCUSSION

Interactions between TMA and PIM-1 during the Precursor Exposure Step. The highly reactive and often pyrophoric nature of VPI precursors makes ascertaining the reaction pathways during the VPI processes challenging without specialized and costly *in situ* chemical characterization techniques. To offer insight into this challenging characterization space, DFT is employed to understand chemical interactions between TMA and PIM-1 during the precursor exposure step (step A in [Figure 1](#)). McGuinness et al.²⁰ previously hypothesized that the primary chemical interaction between TMA and PIM-1 is an adduct formed between the

lone pair on the nitrile group and the aluminum atom on TMA. To evaluate the likelihood of an interaction forming at the nitrile site and determine the probability of interaction with other PIM-1 functional groups, we calculate the interaction energies between TMA and the nitrile, dioxane, and methyl functional groups of PIM-1 ([Figure 2a](#)). The interaction energy is taken as the difference between the relaxed PIM-1+TMA bound state and the isolated PIM-1 and TMA molecules. This energy represents the interaction between one TMA molecule and the PIM-1 system. To find the most likely coordination location, the TMA-(PIM-1) system was allowed to relax by starting the TMA molecule at various initial positions along the PIM-1 segment. Multiple PIM-1 modeled structures (monomer, trimer, and coiled trimer) and TMA orientations at each of these sites were also considered (more information provided in the [Supporting Information](#)).

[Figure 2b](#) plots the interaction energies between PIM-1 and TMA for each of these possible adsorption sites using different optimized PIM-1 models: monomer molecule (black dots), trimer molecule (magenta squares), and coiled trimer molecule (cyan triangles). The coiled trimer molecule was only employed with TMA on the nitrile site to study the morphology effect. Among all possible configurations, we show the most energetically stable ones in [Figure 2](#). Interaction energies with the remaining orientations and starting locations are provided in the [Supporting Information](#). Despite the difference in size and geometry of the PIM-1 models, the nitrile group is always the most stable adsorption site for TMA. The results in [Figure 2b](#) agree with the interactions previously observed between TMA and amine or nitro functional groups in other VPI-related processes⁴⁵ and confirms the portion of the hypothesis presented by McGuinness et al.,²⁰ where nitrile is the most stable site for the chemical interaction between TMA and PIM-1.

Experimentally, *in situ* QCM measurements investigating mass changes during one cycle of TMA VPI into PIM-1 thin films support that a chemical interaction indeed exists between TMA and PIM-1 (although cannot specify the exact chemical nature of this interaction). One cycle was chosen for study as it was found to display a solvent stability similar to those of the two cycles of infiltration presented by McGuinness et al. ([Figure S1](#)).^{19,20} [Figure 3a](#) displays the mass uptake (normalized to the mass of the ~400 nm thick spun cast PIM-1 film) during the precursor sorption (exposure or hold

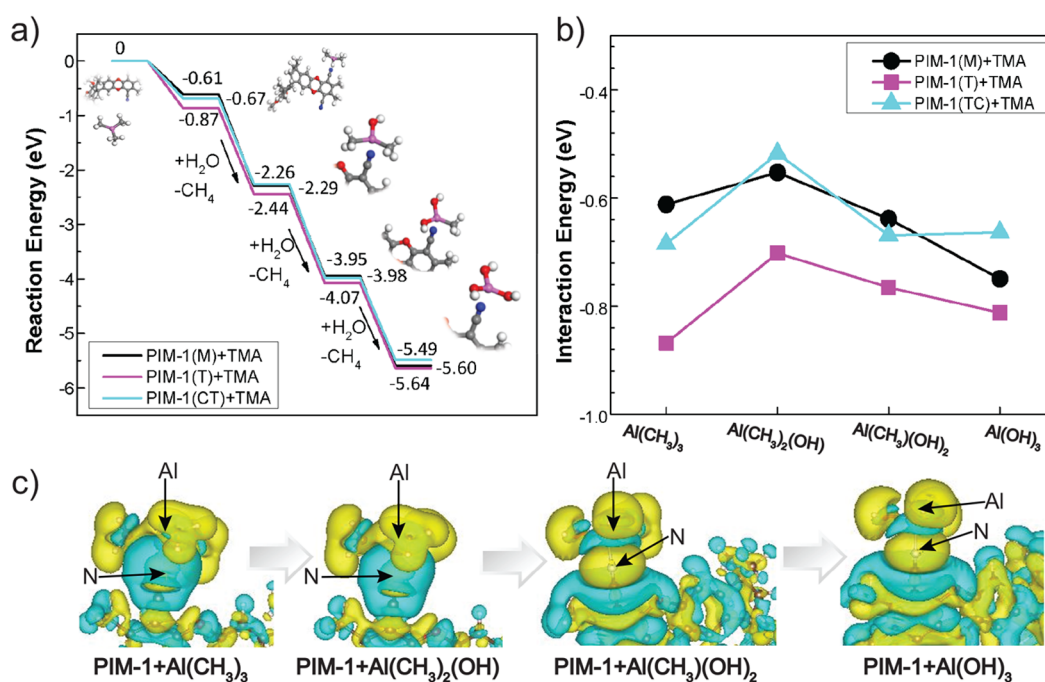


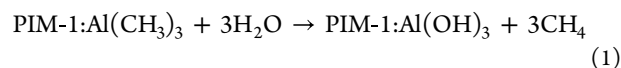
Figure 4. (a) Reaction energy path for the VPI process including the initial sorption and binding of TMA to PIM-1 followed by reactions with three water molecules. (b) Plot of the interaction energy between TMA and PIM-1 as TMA reacts with water to form the metal hydroxide. Calculations are shown for the PIM-1 monomer, the PIM-1 trimer, and the coiled PIM-1 trimer. Note that zero energy is suppressed on the ordinate axis. (c) Electron density difference during the co-reaction with water (isosurface: 0.0002 e/bohr³; positive difference, yellow; negative difference, blue).

step) and desorption (active pumping) stages of the VPI process (before water exposure step). The full mass uptake curve and accompanying pressure profile for the VPI process with detailed discussion is included in the [Supporting Information](#). From the desorption step, 32% of the 0.56 ng total uptake/ng polymer can be attributed to free diffusing TMA within the hybrid whereas the remaining 68% represents TMA that is chemically interacting with PIM-1. The achievement of a steady-state mass during this desorption step indicates that the interaction between PIM-1 and TMA that forms is not readily reversible with time at this temperature. These results provide strong evidence of a significant chemical association forming between PIM-1 and TMA as indicated by the DFT calculations.

To support this lack of desorption across PIM-1 forms and length scales, experiments on PIM-1 hollow fibers were conducted with short and long desorption times. *Ex situ* inorganic distribution (SEM/EDX) under these conditions are shown in [Figure 3b,c](#), revealing a high level of the inorganic distributed evenly throughout PIM-1 even at long desorption times. If TMA was not chemically interacting with PIM-1 and instead kinetically trapped within the polymer, it would still diffuse towards the surface during the 25 h purging, leaving a nonuniform distribution of the inorganic, with higher concentrations near the exterior and lower near the interior.²³ Further, the elemental concentration does not vary significantly between purging times. In addition, *ex situ* TGA of the hollow fibers prepared under long and short purge conditions finds they possess similar inorganic weight percent loadings (SI6). The similarity of these results under both short and long purge conditions complements the QCM data, indicating the interaction between PIM-1 and TMA is strong enough to endure desorption times on the order of a day.

Reactions between TMA-PIM-1 and Water Vapor.

In the next step of the VPI process, the TMA infiltrated PIM-1 is exposed to water vapor where water molecules also sorb into the polymer and react with the precursor within to create the final hybrid material. As the initial reaction pathways of this step are similarly challenging to explore without *in situ* techniques, we use DFT to provide insight into the initial reactions between TMA-PIM-1 and water vapor. We consider the reaction between the coordinated TMA and water to form aluminum hydroxide via



where the TMA-(PIM-1) relaxed structures with the lowest binding energy from [Figure 2b](#) are chosen.

We followed a three-step process, with one water molecule reacting in each step:

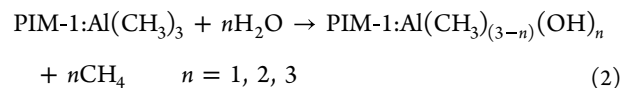


[Figure 4a](#) plots the reaction energies of the VPI process, starting from the isolated PIM-1 and TMA precursor, followed by the TMA-nitrile coordination, and ending with the three-step water co-reaction. During the water co-reaction study, we consider the effect of different methyl replacement sequences with *OH (see the [Supporting Information](#) for more details) and select the average value shown in [Figure 4a](#) (the standard deviation is 0.04 eV). For all PIM-1 models, the reaction is exothermic and follows a similar trend. This is expected as the reaction between TMA and water is known to be extremely exothermic (pyrophoric) in nature. The similarity in the reaction energy pathways for all three molecular configurations

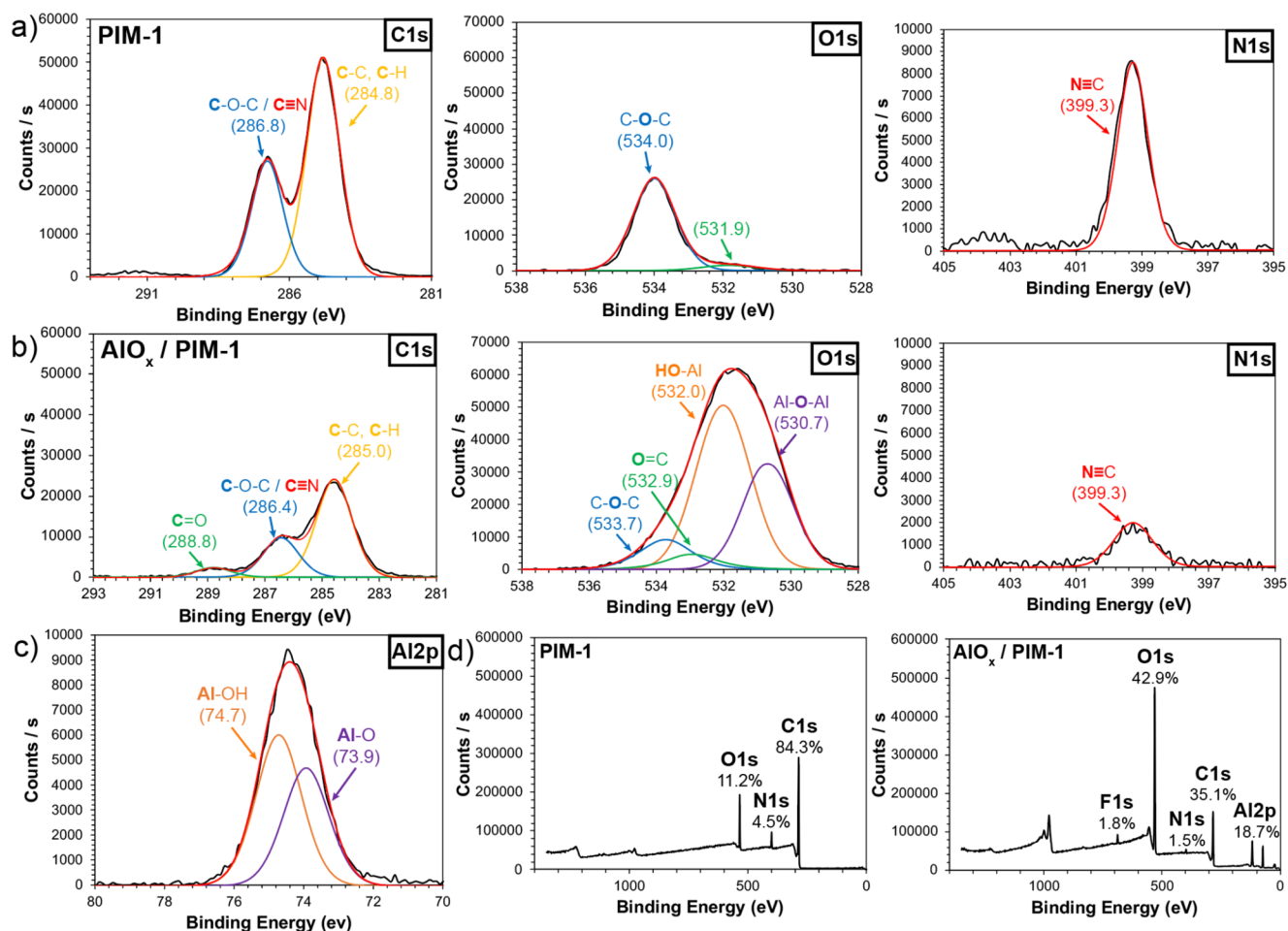


Figure 5. Core level XPS of (a) neat PIM-1 and (b) hybrid AlO_x -PIM-1 after heating on the hot plate for 3 h at 150 °C including carbon 1s, oxygen 1s, and nitrogen 1s. (c) Aluminum 2p core level spectrum for the hybrid AlO_x -PIM-1 film. (d) XPS survey spectra with atomic percentages labeled for both neat PIM-1 and hybrid AlO_x -PIM-1.

considered suggests that one monomer is enough to represent PIM-1 accurately for these studies. The small energy deviations can be ascribed to the approximations used in DFT.

We further studied the variation in the interaction energy between TMA and the nitrile group of PIM-1 during the VPI process (as modeled thus far). Figure 4b plots these interaction energies between each inorganic species and the nitrile group of PIM-1. These results reveal that the interaction energy between PIM-1 and the inorganic varies by no more than 25% as methyl groups are replaced with hydroxyl groups. To further investigate the interactions taking place, the electron density differences of the aluminum structures and the nitrile group of PIM-1 with respect to the isolated species at each step of the VPI process were computed and are displayed in Figure 4c. The electron density difference shows an increased concentration between the nitrogen and aluminum atoms, confirming that TMA and the modeled metal hydroxide species in this section continue to interact with PIM-1's nitrile group throughout this portion of the VPI process.

This result contradicts the hypothesis and spectroscopic evidence presented by McGuinness et al.,²⁰ where they found no significant indications of chemical bonding between the metal oxide (final products after water exposure) and the nitrile group in FTIR, XPS, or solid-state NMR. Additionally, DFT vibrational frequency simulations of this $\text{Al}(\text{OH})_3$

structure demonstrate a bleaching of the peak associated with PIM-1's nitrile group, an observation not seen in the experimental FTIR spectra (details are shown in the Supporting Information). These contradictions suggest that the $\text{Al}(\text{OH})_3$ species shown in Figure 4 is likely not the final inorganic structure in the hybrid membrane. In fact, the QCM results (full QCM data shown in the Supporting Information) following water reaction further support this hypothesis. Assuming the mass uptake at the end of the precursor desorption step results from the interaction of TMA with PIM-1 without the generation of byproducts, the mass uptake after the water exposure and desorption for the hydroxyl should be $\sim 2 \mu\text{g}$. However, the actual mass increase is $\sim 4 \mu\text{g}$, indicating a more hydrated inorganic structure. In the next section, we use a combination of spectroscopic methods, DFT calculations, and chemical deduction to further elucidate this final structure.

Final Products after PIM-1 Infiltration with TMA and Water Vapor. To resolve the final structure of the hybrid AlO_x -PIM-1, FTIR spectra were obtained before and after infiltration of PIM-1 hollow fibers. The raw spectra for these along with a difference spectrum and detailed discussion is presented in Figure S7. The FTIR spectra reveal no significant reduction or modification of the nitrile absorption band of PIM-1 at 2240 cm^{-1} following infiltration.^{47–49} No change in this absorption band suggests that the PIM-1's nitrile group

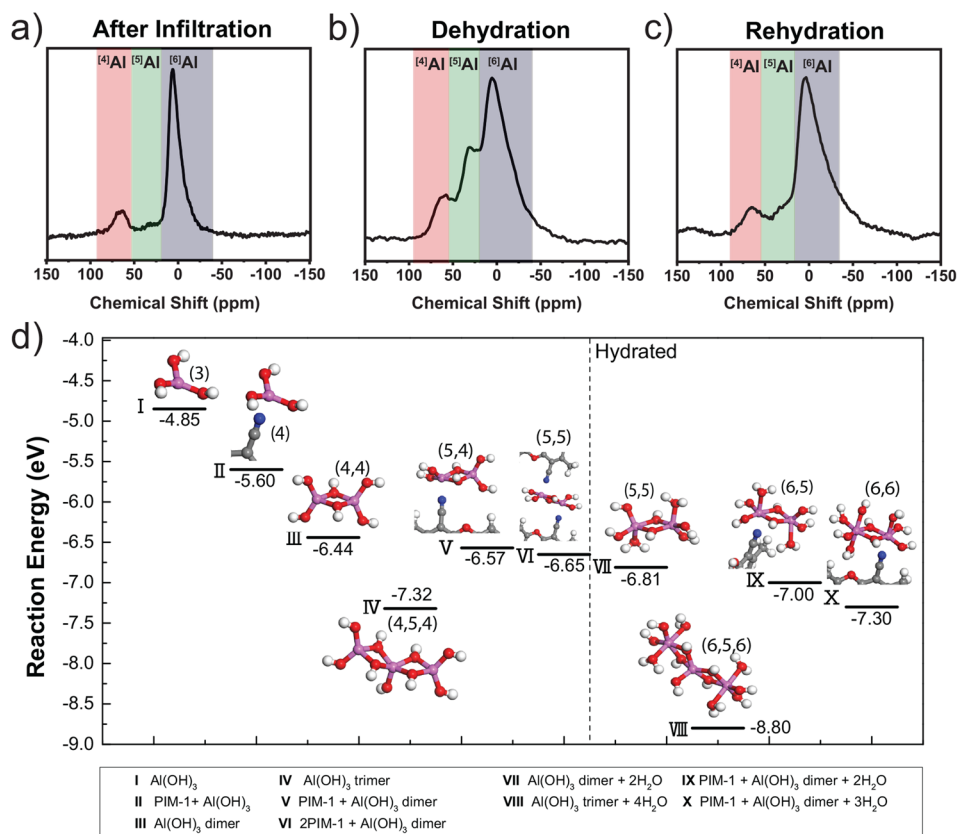


Figure 6. (a) Experimental NMR of AlO_x -PIM after one VPI cycle, (b) after drying the AlO_x -PIM material for 90 min at 110 °C in air, and (c) after rehydrating the AlO_x -PIM-1 material in a humidity chamber at 95% humidity for 12 h (the orange/green/purple shadows mark the peak of 4/5/6-fold coordinated AlO_x). (d) Reaction energy of potential final products $\text{Al}_x\text{O}_y(\text{OH})_z$, in energy decreasing sequence within each species (monomer, dimer, trimer). Species to the right of the dotted line are hydrated structures. The numbers in parentheses beside the structures are the coordination numbers for aluminum atoms, e.g., (5,4) means that the left aluminum is 5-fold coordinated and the right aluminum is 4-fold coordinated.

does not strongly interact with the inorganic in the final hybrid structure. The absorption band for PIM-1's dioxane groups at 1265 cm^{-1} is also relatively unchanged upon infiltration, although it may show a slight reduction in intensity.⁴⁹ Most other absorptions associated with neat PIM-1 are also preserved following infiltration with intensity shifts challenging to deconvolute because of the broad nature of the peaks associated with the inorganic. New absorptions occur throughout the spectrum that are likely because of the structure of the inorganic (Al–O and Al–OH bonding environments of different forms),⁵⁰ but they may also be attributed to alternative structures such as hydrolyzed PIM-1. Because of the lack of specificity of the newly observed absorptions, we turn to additional chemical characterization techniques to provide more evidence about the chemical structure.

The C 1s core level spectrum of the hybrid AlO_x -PIM-1 thin film (Figure 5b) still displays both peaks observed for PIM-1 (Figure 5a) as well as a new peak at 288.8 eV. The new peak corresponds to C=O functionalities that may arise through the formation of aluminum carbonates,⁵¹ CO_2 sorption, hydrolysis of the nitrile functional group into a carboxylic acid,⁴⁹ or the presence of an impurity such as adventitious carbon. In the O 1s core level spectrum of the hybrid thin film, the PIM-1 C–O–C peak at 534 eV is preserved, indicating the continued presence of dioxane functionality in the polymer backbone. New peaks also appear

at 532.9, 532, and 530.7 eV, which are attributed to O=C, HO–Al, and Al–O–Al states, respectively. When considered in conjunction with the Al 2p spectrum (Figure 5c) and the FTIR spectrum, it is evident that the final inorganic structure is composed of an aluminum oxyhydroxide with a significant quantity of hydroxyl functionalities. Overall, the decrease in intensity of the peaks corresponding to neat PIM-1 after infiltration is likely because of the large quantity of the inorganic present. For example, despite a lower signal in the N 1s emission after VPI, the ratio of nitrogen to carbon remains constant, suggesting that nitrile groups are not reacting but simply becoming less prevalent at the surface with the presence of the aluminum inorganic. If a strong interaction (i.e., a covalent bond) persisted between the nitrile functional group of PIM-1 and the resulting inorganic, an energy shift would be expected for the N 1s spectrum emission, but no such energy shift is detectable.⁴⁸ Thus, both XPS and FTIR indicate no strong chemical interactions between the polymer and the inorganic within the final system (i.e., no covalent bonds are formed).

The XPS survey spectra (Figure 5d) provide additional stoichiometric information regarding the inorganic material and show that the Al:O ratio is near 0.49 (details in the Supporting Information). A purely unhydrated Al_2O_3 oxide cluster would have an Al:O ratio of 0.67. This higher oxygen content is consistent with having a hydrated oxide, that is, either an oxyhydroxide or a hydroxide.

To further discern the inorganic structure, it is important to understand the coordination of aluminum in the hybrid material. Therefore, solid-state NMR spectroscopy was employed. Figure 6a displays the solid-state NMR spectra of hybrid AlO_x -PIM-1 infiltrated with TMA and co-reacted with water vapor after one VPI cycle with long purging. The two peaks in this figure, centered at 7 and 66 ppm, correspond to 6- and 4-fold coordinated aluminum species, respectively. The relative intensities of each peak indicate that for the as-synthesized hybrid material, 6-fold coordination is favored over 4-fold coordination. This coordination information can be combined with the need to maintain charge neutrality to help determine possible structures of the inorganic. All elements in this material have well-defined oxidation states and are almost never multivalent. For example, aluminum should have an oxidation state of 3+, oxygen 2-, and hydroxide 1-. The $\text{Al}(\text{OH})_3$ species assumed in the previous section has a 3-fold coordination but could be considered 4-fold coordinated once interacting with PIM-1's nitrile group. Further reaction or coordination formation would be necessary to achieve the dominant 6-fold coordination detected with NMR.

This high level of coordination may be indicative of the formation of inorganic clusters. Metal hydroxides can "grow" into larger inorganic clusters by one of two methods: (1) Two hydroxyl groups could undergo a condensation reaction generating a $\text{M}-\text{O}-\text{M}$ bond and a water byproduct, or (2) a hydroxide group could be shared between two metal hydroxide clusters. In the former case, the bridging oxygen ($\text{M}-\text{O}-\text{M}$) will have a 2- oxidation state and contribute a 1- charge toward each metal ion. In the latter case, the bridging hydroxide ($\text{M}-\text{OH}-\text{M}$) will have an effective 1- oxidation state and contribute $-1/2$ charge toward each metal ion. The $\text{M}-\text{O}-\text{M}$ formation commonly occurs in sol-gel synthesis of metal oxide ceramics.⁵² The $\text{M}-\text{OH}-\text{M}$ bridging is common in metal hydroxide materials, including gibbsite ($\text{Al}(\text{OH})_3$).⁵³ In fact, the formation of multinuclear inorganic clusters during a single cycle of VPI has been experimentally observed previously in the infiltration of PMMA with trimethylindium that has been co-reacted with water vapor, providing additional support for this bridging mechanism.³⁰ In Figure S8 of the Supporting Information we report DFT calculations for several of these possible dimerization reactions. We find that a dimer with two bridging hydroxyls has a significantly lower formation energy in vacuum (-2.43 eV) than the condensation reacted dimer with one bridging $\text{M}-\text{O}-\text{M}$ bond (-0.25 eV) or with two bridging $\text{M}-\text{O}-\text{M}$ bonds ($+1.82$ eV) (see the Supporting Information for details). Other considered structures that included $\text{M}-\text{O}-\text{M}$ bonds show similarly positive formation energies, leading us to surmise that linkages between $\text{Al}(\text{OH})_3$ moieties in this hybrid structure more likely occur via bridging of hydroxyl groups, similar to that observed in the geochemistry of aluminum oxyhydroxide-based minerals.⁵⁴

Interestingly, bridging of hydroxyls increases the coordination of the $\text{Al}(\text{OH})_3$ species without increasing the aluminum ion's oxidation state. For example, when $\text{Al}(\text{OH})_3$ dimerizes, it creates a structure in which both aluminum atoms are coordinated by four oxygen atoms (two hydroxide groups are shared by two aluminum ions), while maintaining their 3+ oxidation state. However, these bridging hydroxyls only increase the coordination to 4. We hypothesize that the experimentally observed 6-fold coordination is the result of either coordination with the PIM-1 polymer or coordination with additional water molecules from the water exposure step.

To obtain further insights into the possible 6-fold coordination structure, we calculated the reaction energies for coordination of these $\text{Al}(\text{OH})_3$ and dimers with PIM-1's nitrile groups and water molecules. A summary of these results is presented in Figure 6d. This figure demonstrates that $\text{Al}(\text{OH})_3$ (I) reduces its energy when it coordinates to PIM-1's nitrile group (II). When two water molecules were added to (II), neither remained associated with the complex, suggesting that further hydration does not increase this structure's stability. Thus, a single $\text{Al}(\text{OH})_3$ moiety does not appear likely to form a 6-fold coordinated structure. However, dimerization of $\text{Al}(\text{OH})_3$ leads to even more energetically stable structures (e.g., (III)). This result implies that the experimentally observed 4-fold and 6-fold coordinated aluminum is likely the result of dimerized or larger inorganic clusters.⁵⁵

To reach 6-fold coordination, four water molecules were added to the dimer and the structure was relaxed. However, the minimum energy structure (VII) retained only two of these water ligands, leaving each aluminum in a 5-fold coordination structure. Next, coordination with a single nitrile group and three water molecules was considered. This condition gives the lowest formation energy complex (X). This lowest energy structure also places both aluminum's in 6-fold coordination. Interestingly, though, other local minima were identified using similar starting conditions (one nitrile ligand and three water molecules) but slight variations in the water location (e.g., in axial rather than equatorial positions). Though these complexes are within 0.2 eV higher in energy, it is possible that under experimental conditions these alternative structures could be achieved. In Figure 6b, dehydration by heating in air at 110 °C for 90 min leads to a large increase in 5-fold coordinated aluminum in the NMR spectrum. This emergence of 5-fold coordination appears consistent with structure (X) being similar in energy and capable of converting to structures (VII) and (IX) (even (V) and (VI)), especially under conditions that would favorably desorb water molecules. To experimentally validate these findings, we rehydrated the dehydrated AlO_x -PIM-1 in a humidity chamber for 12 h at 95% humidity and room temperature and examined the NMR spectrum. Rehydrating the AlO_x -PIM-1, shown in Figure 6c, causes a shift back to primarily 4- and 6-fold coordinated species, suggesting that water is contributing to the coordination of the Al atoms, consistent with the hydrated structures proposed in Figure 6d.

We also considered the case of the $\text{Al}(\text{OH})_3$ dimer bound to two of PIM-1's nitrile groups and two water molecules. For this case, the water molecules again did not remain bound to the complex (VI), suggesting that coordinating with two nitriles can only achieve 5-fold coordination of the aluminum. However, note that this 5-fold coordinated complex is lower in energy than (III), suggesting detection of 5-fold coordination in NMR may also be indicative of the inorganic cluster acting as a "cross-link" between two different nitrile groups. These dehydrated cross-links may also be the reason higher 5-fold coordination is observed in Figure 6b. We also note that the asymmetry of the NMR peaks may suggest variations in the coordination chemistry; that is, each coordination may include different combinations of hydroxyls, water, and/or nitrile coordinating species.

With this new final structure in mind, we calculated the new binding energy of the 6-fold coordinated AlO_x dimer interacting with one PIM-1 monomer (structure X in Figure 6). The interaction energy changes from -0.74 eV for

Al(OH)₃ to -0.31 eV, indicating a weakening of the interaction between the nitrile group and the aluminum once the dimerized, hydrated inorganic is formed. The weakening of this interaction may explain the lack of experimental evidence for detecting binding between the nitrile group of PIM-1 and the aluminum inorganic in the final hybrid membrane.

Finally, inorganic clusters larger than dimers are computationally considered. Structure (VIII) demonstrates that further cluster growth into a trimer continues to lower the system's overall energy because of the additional bond formation. Interestingly, hydration of these trimer clusters is often stable (water molecules stay attached). Meanwhile, in (VIII), two of the three aluminums are 6-fold coordinated and the third is only 5-fold coordinated, suggesting that some form of nitrile coordination may again be necessary to achieve full 6-fold coordination. Notably, there is no 3-fold coordinated Al after the dehydration (NMR). For the modeled structures, it is essential to maintain coordination with the PIM-1 polymer for the final AlO_x species to keep the minimum coordination number as 4. While, we have not extensively explored all possible trimer or larger structures, these preliminary data suggest that larger chains or sheets of inorganic clusters could possibly be forming further reducing the aluminum-nitrile coordination.

The XPS results in Figure 5 indicate the presence of both Al–OH and Al–O–Al bonds, corresponding to a more boehmite-type structure (mixture of Al–OH and Al–O–Al) than a gibbsite structure (all Al–OH), as have been found to be the lowest energy clusters via DFT here. In the phase diagrams for hydrated aluminas, gibbsite is known to transform to boehmite at higher temperatures. The exact temperature of this transition is not well-defined and depends strongly on attributes of the inorganic such as particle size, crystallinity, heating rates, and environmental factors.^{56,57} Because DFT simulations consider restricted cluster configurations and small clusters that are only reminiscent of the experimentally observed phases (see the Supporting Information, e.g., Figure S10, for clusters with a range of Al:O stoichiometric ratios explored here), the correct energetic ordering of various phases cannot always be fully predicted unambiguously, especially as a function of cluster sizes. In the true experimental system, it is likely that these inorganic clusters have sufficient energy to transition from gibbsite-like to boehmite-like structures. The structural similarities between these phases further adds to the ease of this transition. Additionally, heating the samples prior to XPS may induce structural changes in the material by driving off water and forming the less hydrated boehmite state.

In considering this new information about the inorganic's physicochemical structure, we can postulate on two potential mechanisms for this AlO_x/PIM-1 hybrid membrane's solvent stability originally reported by McGuinness et al.²⁰ The first being the continued, albeit weak, interaction of the polymer with the inorganic phase which may lead to anchoring or cross-linking behavior, even though the interaction gets weakened after the hydration. The second being the formation of larger, "networked" inorganic structures intertwining with the polymer that acts to prevent polymer chain reptation and leads to a material that is kinetically frustrated from dissolving in otherwise good solvents for the polymer.

CONCLUSIONS

A study interweaving findings from both computations and experimental characterization was conducted to investigate the

reaction pathways and final hybrid material structures in the vapor-phase infiltration of PIM-1 with TMA and co-reaction with water vapor. As a result of this work, two mechanisms for the observed property of solvent stability are proposed.

DFT explorations of varying PIM-1 and TMA models provided insight into steps of the VPI process that are challenging to evaluate without the use of expensive *in situ* capabilities. These results indicate that during the precursor exposure step TMA interacts most significantly with the nitrile group of PIM-1 with a binding energy similar to that for a metal–ligand coordination. *In situ* QCM measurements featuring long desorption times, which characterized the system before water exposure, and SEM/EDX results support the presence of a significant interaction between the TMA precursor and PIM-1 polymer. During the water vapor exposure step of the VPI process, a simulated energy path replacing the methyl ligands of TMA with hydroxyls reveals the exothermic nature of these reactions. Throughout this portion of the process, an energetically stable interaction is maintained between PIM-1 and the inorganic species.

However, *ex situ* chemical characterization (of the system after VPI) indicates the Al(OH)₃ structure is not the final structure of the inorganic. Rather, the final structure of the inorganic is experimentally found to be an aluminum oxyhydroxide primarily consisting of 6-fold coordinated aluminum atoms. With further computational study, DFT calculations suggest that this structure is likely to be composed of inorganic clusters containing bridging hydroxyl groups rather than M–O–M bonds. On the basis of both DFT calculations and experimental measurements, aluminum's 6-fold coordination appears to require a combination of coordination with PIM-1's nitrile functional groups and hydration with water ligands, although both computational results and experimental evidence support at post a weak interaction between the polymer and the inorganic. These results also suggest that the inorganic clusters have the potential to grow into even larger chains or possibly even sheets. Further, the current work highlights two likely mechanisms for the solvent stability of hybrid AlO_x/PIM-1 membranes: (1) weak chemical association between the inorganic and the polymer leading to anchoring or even cross-linking of polymer chains and/or (2) growth of larger polymeric inorganic structures that prevent reptation of polymer segments. Overall, this work provides a framework for iterating between experimental and computational methods to overcome challenges present for each method alone, thus efficiently and effectively improve predictions of VPI processes and the chemical structure of the resultant hybrid materials.

ASSOCIATED CONTENT

Supporting Information

The Supporting Information is available free of charge at <https://pubs.acs.org/doi/10.1021/acs.jpcc.2c01928>.

Experimental methods, influence of VPI processing parameters on the solvent stability of hybrid AlO_x/PIM-1 polymer membranes, PIM-1 models with density functional theory, interaction energy details, *in situ* quartz crystal microbalance gravimetry of the infiltration of PIM-1 with TMA, *ex situ* TGA of AlO_x/PIM-1 hollow fibers with varying desorption times, connection with vibrational spectroscopy, influence of the methyl substitution sequence in TMA during water co-

reactions. additional information from XPS, and aluminum hydroxide molecules study (PDF)

AUTHOR INFORMATION

Corresponding Authors

Mark D. Losego – School of Materials Science and Engineering, Georgia Institute of Technology, Atlanta, Georgia 30332, United States; orcid.org/0000-0002-9810-9834; Email: losego@gatech.edu

Rampi Ramprasad – School of Materials Science and Engineering, Georgia Institute of Technology, Atlanta, Georgia 30332, United States; orcid.org/0000-0003-4630-1565; Email: rampi.ramprasad@mse.gatech.edu

Authors

Yifan Liu – School of Materials Science and Engineering, Georgia Institute of Technology, Atlanta, Georgia 30332, United States; orcid.org/0000-0001-5102-0552

Emily K. McGuinness – School of Materials Science and Engineering, Georgia Institute of Technology, Atlanta, Georgia 30332, United States; orcid.org/0000-0003-4896-248X

Benjamin C. Jean – School of Materials Science and Engineering, Georgia Institute of Technology, Atlanta, Georgia 30332, United States

Yi Li – School of Materials Science and Engineering, Georgia Institute of Technology, Atlanta, Georgia 30332, United States

Yi Ren – School of Chemical & Biomolecular Engineering, Georgia Institute of Technology, Atlanta, Georgia 30332-0100, United States; orcid.org/0000-0002-1135-2082

Beatriz G. del Rio – School of Materials Science and Engineering, Georgia Institute of Technology, Atlanta, Georgia 30332, United States; orcid.org/0000-0002-1641-8407

Ryan P. Lively – School of Chemical & Biomolecular Engineering, Georgia Institute of Technology, Atlanta, Georgia 30332-0100, United States; orcid.org/0000-0002-8039-4008

Complete contact information is available at: <https://pubs.acs.org/10.1021/acs.jpcb.2c01928>

Notes

The authors declare no competing financial interest.

ACKNOWLEDGMENTS

This material is based upon work supported by the National Science Foundation (DMREF-1921873). E.K.M. was supported by the Department of Defense (DoD) through the National Defense Science & Engineering Graduate (NDSEG) Fellowship Program. Part of this research was conducted in Georgia Tech's Materials Innovation & Learning Laboratory (The MILL), an uncommon "make and measure" space committed to elevating undergraduate research in materials science.

REFERENCES

- (1) Sholl, D. S.; Lively, R. P. Seven Chemical Separations to Change the World. *Nature* **2016**, *532*, 435–437.
- (2) Koh, D.-Y.; McCool, B. A.; Deckman, H. W.; Lively, R. P. Reverse Osmosis Molecular Differentiation of Organic Liquids Using Carbon Molecular Sieve Membranes. *Science* **2016**, *353*, 804–807.
- (3) Kim, D.; Jeon, M. Y.; Stottrup, B. L.; Tsapatsis, M. Para-Xylene Ultra-selective Zeolite MFI Membranes Fabricated from Nanosheet Monolayers at the Air-Water Interface. *Angew. Chem., Int. Ed.* **2018**, *57*, 480–485.
- (4) Zhu, G.; Zhang, F.; Rivera, M. P.; Hu, X.; Zhang, G.; Jones, C. W.; Lively, R. P. Molecularly Mixed Composite Membranes for Advanced Separation Processes. *Angew. Chem., Int. Ed.* **2019**, *58*, 2638–2643.
- (5) Sorribas, S.; Gorgojo, P.; Téllez, C.; Coronas, J.; Livingston, A. G. High Flux Thin Film Nanocomposite Membranes Based on Metal-Organic Frameworks for Organic Solvent Nanofiltration. *J. Am. Chem. Soc.* **2013**, *135*, 15201–15208.
- (6) Jimenez-Solomon, M.; Song, Q.; Jelfs, K.; Munoz-Ibanez, M.; Livingston, A. Polymer Nanofilms with Enhanced Microporosity by Interfacial Polymerization. *Nat. Mater.* **2016**, *15*, 760–767.
- (7) Marchetti, P.; Jimenez Solomon, M. F.; Szekely, G.; Livingston, A. G. Molecular Separation with Organic Solvent Nanofiltration: A Critical Review. *Chem. Rev.* **2014**, *114*, 10735–10806.
- (8) Ma, Y.; Zhang, F.; Yang, S.; Lively, R. P. Evidence for Entropic Diffusion Selection of Xylene Isomers in Carbon Molecular Sieve Membranes. *J. Membr. Sci.* **2018**, *564*, 404–414.
- (9) Koh, D.-Y.; Lively, R. P. Nanoporous Graphene: Membranes at the Limit. *Nat. Nanotechnol.* **2015**, *10*, 385–386.
- (10) Cook, M.; Gaffney, P.; Peeva, L.; Livingston, A. Roll-to-roll Dip Coating of Three Different PIMs for Organic Solvent Nanofiltration. *J. Membr. Sci.* **2018**, *558*, 52–63.
- (11) McKeown, N. Polymers of Intrinsic Microporosity. *ISRN* **2012**, *2012*, 513986.
- (12) Fritsch, D.; Merten, P.; Heinrich, K.; Lazar, M.; Priske, M. High Performance Organic Solvent Nanofiltration Membranes: Development and Thorough Testing of Thin Film Composite Membranes Made of Polymers of Intrinsic Microporosity (PIMs). *J. Membr. Sci.* **2012**, *401–402*, 222–231.
- (13) Zhang, F.; Ma, Y.; Liao, J.; Breedveld, V.; Lively, R. P. Solution-Based 3D Printing of Polymers of Intrinsic Microporosity. *Macromol. Rapid Commun.* **2018**, *39*, 1800274.
- (14) Azpitarte, I.; Knez, M. Vapor Phase Infiltration: from a Bioinspired Process to Technologic Application, a Prospective Review. *MRS Commun.* **2018**, *8*, 727–741.
- (15) Subramanian, A.; Tiwale, N.; Nam, C. Y. Review of Recent Advances in Applications of Vapor-Phase Material Infiltration Based on Atomic Layer Deposition. *JOM* **2019**, *71*, 185–196.
- (16) Yang, H. C.; Waldman, R. Z.; Chen, Z.; Darling, S. B. Atomic Layer Deposition for Membrane Interface Engineering. *Nanoscale* **2018**, *10*, 20505–20513.
- (17) Waldman, R. Z.; Mandia, D. J.; Yanguas-Gil, A.; Martinson, A. B. F.; Elam, J. W.; Darling, S. B. The chemical Physics of Sequential Infiltration Synthesis: A Thermodynamic and Kinetic Perspective. *J. Chem. Phys.* **2019**, *151*, 190901.
- (18) Ashurbekova, K.; Ashurbekova, K.; Botta, G.; Yurkevich, O.; Knez, M. Vapor Phase Processing: A Novel Approach for Fabricating Functional Hybrid Materials. *Nanotechnol* **2020**, *31*, 342001.
- (19) Leng, C. Z.; Losego, M. D. Vapor Phase Infiltration (VPI) for Transforming Polymers into Organic-inorganic Hybrid Materials: A Critical Review of Current Progress and Future Challenges. *Mater. Horiz.* **2017**, *4*, 747–771.
- (20) McGuinness, E. K.; Zhang, F.; Ma, Y.; Lively, R. P.; Losego, M. D. Vapor Phase Infiltration of Metal Oxides into Nanoporous Polymers for Organic Solvent Separation Membranes. *Chem. Mater.* **2019**, *31*, 5509–5518.
- (21) Bergsman, D.; Getachew, B.; Cooper, C.; Grossman, J. Preserving Nanoscale Features in Polymers during Laser Induced Graphene Formation using Sequential Infiltration Synthesis. *Nat. Commun.* **2020**, *11*, 3636.
- (22) Ogieglo, W.; Puspasari, T.; Hota, M.; Wehbe, N.; Alshareef, H.; Pinnau, I. Nanohybrid Thin-film Composite Carbon Molecular Sieve Membranes. *Mater. Today Nano* **2020**, *9*, 100065.
- (23) Leng, C. Z.; Losego, M. D. A Physicochemical Processing Kinetics Model for the Vapor Phase Infiltration of Polymers:

Measuring the Energetics of Precursor-polymer Sorption, Riffusion, and reaction. *Phys. Chem. Chem. Phys.* **2018**, *20*, 21506–21514.

(24) Caligiore, F. E.; Nazzari, D.; Cianci, E.; Sparnacci, K.; Laus, M.; Perego, M.; Seguíni, G. Effect of the Density of Reactive Sites in P(S-r-MMA) Film during Al₂O₃ Growth by Sequential Infiltration Synthesis. *Adv. Mater. Interfaces* **2019**, *6*, 1900503.

(25) Hill, G. T.; Lee, D. T.; Williams, P. S.; Needham, C. D.; Dandley, E. C.; Oldham, C. J.; Parsons, G. N. Insight on the Sequential Vapor Infiltration Mechanisms of Trimethylaluminum with Poly(methyl methacrylate), Poly(vinylpyrrolidone), and Poly(acrylic acid). *J. Phys. Chem. C* **2019**, *123*, 16146–16152.

(26) Dandley, E. C.; Needham, C. D.; Williams, P. S.; Brozina, A. H.; Oldham, C. J.; Parsons, G. N. Temperature-dependent Reaction Between Trimethylaluminum and Poly(methyl methacrylate) during Sequential Vapor Infiltration: Experimental and Ab Initio Analysis. *J. Mater. Chem. C* **2014**, *2*, 9416–9424.

(27) Biswas, M.; Libera, J. A.; Darling, S. B.; Elam, J. W. Kinetics for the Sequential Infiltration Synthesis of Alumina in Poly(methyl methacrylate): An Infrared Spectroscopic Study. *J. Phys. Chem. C* **2015**, *119*, 14585–14592.

(28) Elam, J. W.; Biswas, M.; Darling, S.; Gil, A. Y.; Emery, J. D.; Peng, Q.; Winterstein, J. New Insights into Sequential Infiltration Synthesis. *ECS Trans.* **2015**, *69*, 147.

(29) Weisbord, I.; Shomrat, N.; Azoulay, R.; Kaushansky, A.; Segal-Peretz, T. Understanding and Controlling Polymer-Organometallic Precursor Interactions in Sequential Infiltration Synthesis. *Chem. Mater.* **2020**, *32*, 4499–4508.

(30) He, X.; Waldman, R. Z.; Mandia, D. J.; Jeon, N.; Zaluzec, N. J.; Borkiewicz, O. J.; Ruett, U.; Darling, S. B.; Martinson, A. B. F.; Tiede, D. M. Resolving the Atomic Structure of Sequential Infiltration Synthesis Derived Inorganic Clusters. *ACS Nano* **2020**, *14*, 14846–14860.

(31) Yang, F.; Brede, J.; Ablat, H.; Abadia, M.; Zhang, L.; Rogero, C.; Elliott, S. D.; Knez, M. Reversible and Irreversible Reactions of Trimethylaluminum with Common Organic Functional Groups as a Model for Molecular Layer Deposition and Vapor Phase Infiltration. *Adv. Mater. Interfaces* **2017**, *4*, 1700237.

(32) Weisbord, I.; Shomrat, N.; Azoulay, R.; Kaushansky, A.; Segal-Peretz, T. Understanding and Controlling Polymer-Organometallic Precursor Interactions in Sequential Infiltration Synthesis. *Chem. Mater.* **2020**, *32*, 4499–4508.

(33) Kresse, G.; Hafner, J. Ab Initio Molecular Dynamics for Liquid Metals. *Phys. Rev. B* **1993**, *47*, 558–561.

(34) Kresse, G.; Furthmüller, J. Efficiency of Ab-initio Total Energy Calculations for Metals and Semiconductors Using A Plane-wave Basis Set. *Comput. Mater. Sci.* **1996**, *6*, 15–50.

(35) Kresse, G. Ab initio Molekular Dynamik für flüssige Metalle. *Ph.D. thesis*, Technische Universität Wien, 1993.

(36) Kresse, G.; Furthmüller, J. Efficient Iterative Schemes for Ab Initio Total-energy Calculations Using A Plane-wave Basis Set. *Phys. Rev. B* **1996**, *54*, 11169.

(37) Kresse, G.; Joubert, D. From Ultrasoft Pseudopotentials to the Projector Augmented-wave Method. *Phys. Rev. B* **1999**, *59*, 1758–1775.

(38) Perdew, J. P.; Burke, K.; Ernzerhof, M. Generalized Gradient Approximation Made Simple. *PRL* **1996**, *77*, 3865–3868.

(39) Lee, K.; Murray, E. D.; Kong, L.; Lundqvist, B. I.; Langreth, D. C. Higher-accuracy van der Waals Density Functional. *Phys. Rev. B* **2010**, *82*, 081101.

(40) Woods, L. M.; Dalvit, D. A. R.; Tkatchenko, A.; Rodriguez-Lopez, P.; Rodriguez, A. W.; Podgornik, R. Materials Perspective on Casimir and van der Waals Interactions. *Rev. Mod. Phys.* **2016**, *88*, 045003.

(41) Liu, C.-S.; Pilania, G.; Wang, C.; Ramprasad, R. How Critical Are the van der Waals Interactions in Polymer Crystals? *J. Phys. Chem. A* **2012**, *116*, 9347–9352.

(42) Larsen, G. S.; Lin, P.; Hart, K. E.; Colina, C. M. Molecular Simulations of PIM-1-like Polymers of Intrinsic Microporosity. *Macromolecules* **2011**, *44*, 6944–6951.

(43) Piercy, B. D.; Losego, M. D. Tree-based Control Software for Multilevel Sequencing in Thin Film Deposition applications. *J. Vac. Sci. Technol. B* **2015**, *33*, 043201.

(44) Jue, M. L.; McKay, C. S.; McCool, B. A.; Finn, M. G.; Lively, R. P. Effect of Nonsolvent Treatments on the Microstructure of PIM-1. *Macromolecules* **2015**, *48*, 5780–5790.

(45) Yang, F.; Brede, J.; Ablat, H.; Abadia, M.; Zhang, L.; Rogero, C.; Elliott, S. D.; Knez, M. Reversible and Irreversible Reactions of Trimethylaluminum with Common Organic Functional Groups as a Model for Molecular Layer Deposition and Vapor Phase Infiltration. *Adv. Mater. Interfaces* **2017**, *4*, 1700237.

(46) Samanta, S.; Kim, S.; Saito, T.; Sokolov, A. P. Polymers with Dynamic Bonds: Adaptive Functional Materials for a Sustainable Future. *J. Phys. Chem. B* **2021**, *125*, 9389–9401.

(47) Li, F. Y.; Xiao, Y.; Chung, T.-S.; Kawi, S. High-Performance Thermally Self-Cross-Linked Polymer of Intrinsic Microporosity (PIM-1) Membranes for Energy Development. *Macro-molecules* **2012**, *45*, 1427–1437.

(48) Zhao, H.; Xie, Q.; Ding, X.; Chen, J.; Hua, M.; Tan, X.; Zhang, Y. High Performance Post-modified Polymers of Intrinsic Microporosity (PIM-1) Membranes Based on Multivalent Metal Ions for Gas Separation. *J. Membr. Sci.* **2016**, *514*, 305–312.

(49) Satilmis, B.; Budd, P. M. Base-catalysed Hydrolysis of PIM-1: Amide Versus Carboxylate Formation. *RSC Adv.* **2014**, *4*, 52189–52198.

(50) Klopogge, J. T.; Ruan, H. D.; Frost, R. L. Thermal Decomposition of Bauxite Minerals: Infrared Emission Spectroscopy of Gibbsite, Boehmite and Diaspore. *J. Mater. Sci.* **2002**, *37*, 1121–1129.

(51) Willis, S. A.; McGuinness, E. K.; Li, Y.; Losego, M. D. Re-examination of the Aqueous Stability of Atomic Layer Deposited (ALD) Amorphous Alumina (Al₂O₃) Thin Films and the Use of a Postdeposition Air Plasma Anneal to Enhance Stability. *Langmuir* **2021**, *37*, 14509–14519.

(52) Brinker, C. J.; Scherer, G. W. In *Sol-Gel Science*; Brinker, C. J., Scherer, G. W., Eds.; Academic Press: San Diego, 1990; pp 20–95.

(53) Gale, J. D.; Rohl, A. L.; Milman, V.; Warren, M. C. An ab Initio Study of the Structure and Properties of Aluminum Hydroxide: Gibbsite and Bayerite. *J. Phys. Chem. B* **2001**, *105*, 10236–10242.

(54) Kubicki, J. D.; Apitz, S. E. Molecular Cluster Models of Aluminum Oxide and Aluminum Hydroxide Surfaces. *Am. Mineral.* **1998**, *83*, 1054–1066.

(55) Zhang, X.; Huestis, P. L.; Pearce, C. I.; Hu, J. Z.; Page, K.; Anovitz, L. M.; Aleksandrov, A. B.; Prange, M. P.; Kerisit, S.; Bowden, e. a.; Mark, E. Boehmite and Gibbsite Nanoplates for the Synthesis of Advanced Alumina Products. *ACS Appl. Nano Mater.* **2018**, *1*, 7115–7128.

(56) Lee, H.; Jeon, Y.; Lee, S. U.; Sohn, D. Temperature Effect on the Synthesis of Gibbsite and Boehmite. *Chem. Lett.* **2013**, *42*, 1463–1465.

(57) Laubengayer, A. W.; Weisz, R. S. A Hydrothermal Study of Equilibria in the System AluminaWater1. *J. Am. Chem. Soc.* **1943**, *65*, 247–250.